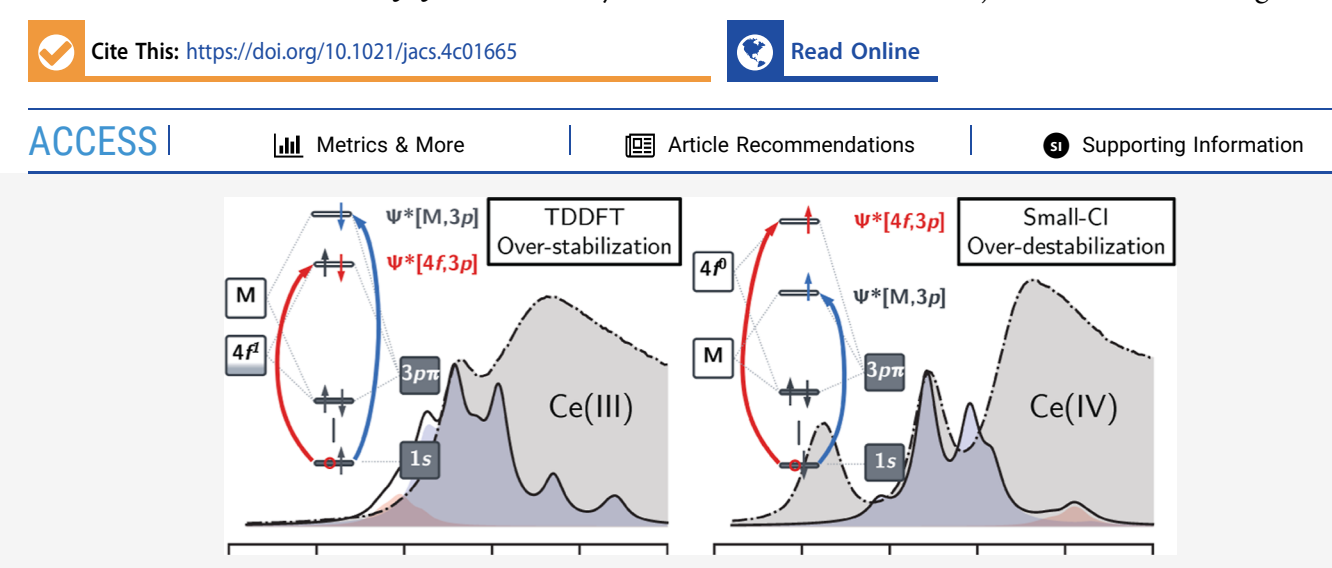


pubs.acs.org/JACS Article

Overdestabilization vs Overstabilization in the Theoretical Analysis of f-Orbital Covalency

Kirill D. Shumilov, Andrew J. Jenkins, Henry S. La Pierre,* Bess Vlaisavljevich,* and Xiaosong Li*



ABSTRACT: The complex nature of the f-orbital electronic structures and their interaction with the chemical environment pose significant computational challenges. Advanced computational techniques that variationally include scalar relativities and spin—orbit coupling directly at the molecular orbital level have been developed to address this complexity. Among these, variational relativistic multiconfigurational multireference methods stand out for their high accuracy and systematic improvement in studies of f-block complexes. Additionally, these advanced methods offer the potential for calibrating low-scaling electronic structure methods such as density functional theory. However, studies on the Cl K-edge X-ray absorption spectra of the $[Ce(III)Cl_6]^{3-}$ and $[Ce(IV)Cl_6]^{2-}$ complexes show that time-dependent density functional theory with approximate exchange—correlation kernels can lead to inaccuracies, resulting in an overstabilization of 4f orbitals and incorrect assessments of covalency. In contrast, approaches utilizing small active space wave function methods may understate the stability of these orbitals. The results herein demonstrate the need for large active space, multireference, and variational relativistic methods in studying f-block complexes.

1. INTRODUCTION

Lanthanides and their derivative materials play an important role in numerous modern technologies and processes. These elements are also central to developing applications of molecular nanomagnets including single-molecule magnets and molecular qubits and to enhancing the efficiency of solar cells. Therefore, understanding the intricate nature of chemical bonding in lanthanide complexes, specifically any covalent interactions involving valence d- and f-orbitals, remains a central problem for the community. Comprehensive understanding of the bonding further elucidates the fundamental properties of lanthanides and paves the way for the advancement of their multifaceted roles in technological applications.

Lanthanides have been generally understood to form ionic bonds based on optical spectroscopy, especially in their typical oxidation state, Ln(III). This bonding model is attributed to the core-like characteristics of the 4f-orbitals, which exhibit limited spatial extension and are minimally affected by the surrounding ligand field. However, recent advancements in spectroscopic measurements and electronic structure

calculations have provided compelling evidence that lanthanides can indeed engage in some covalent interactions involving both 5d- and 4f-orbitals. However, it has been demonstrated that the covalent portion of the bonding is dominated by d-orbital contributions, while the precise role and magnitude of the f-orbital participation remain an area of ongoing investigation. 25,26,29–31

A widely used tool to investigate and quantify the nature of covalency is ligand K-edge X-ray absorption spectroscopy (XAS). For instance, examining the Cl ligand K-edge reveals a pre-edge attributed to dipole-allowed 1s \rightarrow 3p transitions from the chlorine ligands (Figure 1). When the bonding is purely ionic, no pre-edge peaks are observed. When

Received: February 1, 2024 Revised: April 5, 2024 Accepted: April 8, 2024



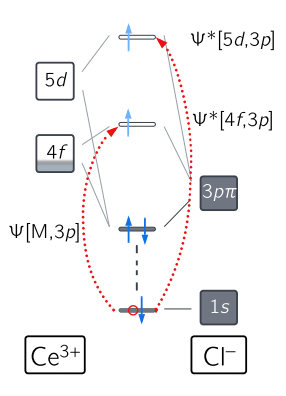


Figure 1. Simplified model orbital diagram of a lanthanide molecular complex, depicting electron excitation in the XAS experiment.

orbital mixing is present, pre-edge features at a lower energy arise from transitions into vacant metal-centered orbitals. These orbitals are hybridized linear combinations of metal d (or f) orbitals and the ligand 3p orbitals, commonly denoted as $\Psi[M, 3p]$, where M is either 4f or 5d for lanthanides. The characteristics of these spectral peaks, including their energy positions and intensities, offer sensitive insights into the covalent character of the ligand—metal molecular orbitals. These measurements are also invaluable for assessing the performance of computational modeling. Both the position of the peaks and peak separation can be used to determine to what extent a method recovers electron correlation.

Historically, time-dependent density functional theory (TDDFT) has also been used to aid in the interpretation of experimental spectra of transition metals, ^{32,34-40} lanthanides, ^{25,31,41,42} and actinide complexes. ^{43,44} Although TDDFT has an intrinsic reliance on a single-determinant basis and approximate exchange-correlation functional, which can compromise its reliability to accurately characterize the spectra of lanthanide-based materials, this approach has been used successfully to establish connections between pre-edge features to models of both orbital overlap and orbital degeneracy. 25,32,41 The f-element community has used these relatively simple models to extend the concept of covalency to a more nuanced discussion in the literature. While these complexes are notable for their open-shell, multireference wave functions, the predominately ionic Ln-Cl bonds also require careful treatment of dispersion (or dynamical correlation) to accurately predict XAS spectra. Moreover, the impact of density localization, which is dependent on the exchangecorrelation functional and on computed metrics for bond covalency in lanthanide systems, remains an open question. To address some of these challenges, multiconfigurational methods with perturbative spin-orbit coupling have been employed. 24,41,45 Yet, it is important to note that due to the high computational demands, these methods are often applied with a limited active space, which may not fully capture dynamic correlation effects.

Experimental and TDDFT Cl K-edge spectra of $[CeCl_6]^n$ for n=2 or 3 were reported in 2015.²⁵ In the Cl K-edge spectrum of the Ce(IV) complex, $[CeCl_6]^{2-}$, the pre-edge features at 2823.6 and 2820.6 eV were assigned as $1s[Cl] \rightarrow \Psi^*[4f, 3p]$ and $1s[Cl] \rightarrow \Psi^*[5d, 3p]$ transitions, respectively. On the other hand, only one clear pre-edge peak was present at 2822.8 eV in the spectrum of $[Ce(III)Cl_6]^{3-}$, but a shoulder at 2824.0 eV was tentatively assigned to $1s[Cl] \rightarrow \Psi^*[4f, 3p]$

transitions based on TDDFT results. This small but non-negligible contribution to covalent bonding from the 4f orbitals was supported by comparisons to the spectra and 4f-orbital energies of other Ln chloride complexes, $[LnCl_6]^{3-}$, where Ln = Nd, Sm, Eu, and Gd. The authors also noted that when comparing Ce(III) to Ce(IV), there was a little impact on the magnitude of the mixing between the Cl 3p and the Ce 5d orbitals. However, there was marked increase in 4f-orbital mixing in the Ce(IV) system compared to the Ce(III) system.

These peak assignments were based on scalar relativistic DFT (B3LYP) calculations using a pseudopotential basis set.²⁵ Given the small percentages that the 4f orbitals contribute to bonding, we posed the question of how improving the treatment of relativistic corrections, spin-orbit coupling, and both dynamic and static correlations could impact the resulting spectra. Specifically, we employ advanced relativistic electronic structure methods, 38,46,47 which incorporate both spin-orbit coupling and scalar relativistic effects, to analyze the XAS spectra of cerium hexachloride complexes, $[CeCl_6]^{n-}$, where n = 2 or 3. To avoid errors stemming from a restricted stateinteraction space, we opt for a fully variational treatment of spin-orbit coupling at the molecular orbital level rather than using a perturbative treatment. These methods were not available in 2015 when the spectra were measured, and modeling these spectra continues to present a challenge for the community. In this work, we utilize exact-two-component TDDFT (X2C-TDDFT)^{38,46} and multireference configuration interaction (X2C-MRCI)^{46,47} methods to assess computational errors associated with strong correlation and density localization/delocalization. Our aim is to offer a comprehensive understanding of bond covalency and the assignment of ligand K-edge XAS spectra of lanthanide complexes.

2. MOLECULAR ORBITAL DIAGRAM

Both the X2C-TDDFT and X2C-MRCI methods rely on a set of reference molecular orbitals (i.e., the set of orbitals in which the excitations of interest occur). While these electronic structure calculations are grounded in variational relativistic molecular orbitals, we find that a conventional nonrelativistic framework offers a more chemically insightful way to depict the spatial partitioning and computational underpinnings. The molecular orbital diagram of $[CeCl_6]^{n-}$ (where n=2 or 3) in an octahedral ligand field without considering spin—orbit coupling is schematically presented in Figure 2. In an octahedral point group, the Ce 4f and 5d orbitals are split into subsets of $a_{2u} \oplus t_{2u} \oplus t_{1u}$ and $t_{2g} \oplus e_g$, respectively. The a_{2u} orbital remains isolated, as it is not permitted by symmetry to engage in interactions with any other orbitals from either Ce or Cl.

The valence 3p orbitals of the six chloride ligands form 6 σ and 12 π orbitals (3p σ and 3p π), which further split into $a_{1g} \oplus e_g \oplus t_{1u}$ and $t_{1u} \oplus t_{1g} \oplus t_{2u} \oplus t_{2g}$, respectively. The 3p σ orbitals have the strongest interaction with the Ce atom and are consequently the lowest in energy. Among the four 3p π irreps, the metal orbitals do not have the appropriate symmetry to interact with the t_{1g} orbitals. In contrast, 3p σ orbitals with t_{1u} or t_{2u} symmetry can mix with Ce 4f orbitals, while those with t_{2g} symmetry can mix with the Ce 5d orbitals. Additionally, the 3p π orbital with t_{1u} symmetry can interact further with the Ce 5p and 6p σ orbitals, which slightly destabilizes it.

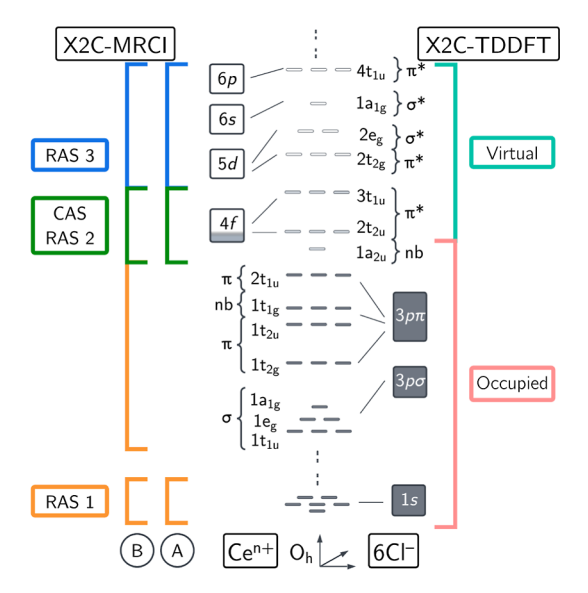


Figure 2. (Center) molecular orbital diagram of $[CeCl_6]^{n-}$ where n=2 or 3 in an octahedral field. (Left) definition of the restricted active spaces in different X2C-MRCI schemes. (Right) definition of "occupied" and "virtual" spaces for X2C-TDDFT.

Within this orbital space, excitations between the occupied and empty (or virtual) orbitals are computed, corresponding to the transitions occurring in XAS experiments. In X2C-TDDFT calculations, all molecular spinor orbitals are included in the linear response formalism, where only single-electron excitations are allowed from the occupied to the virtual space. In contrast to the simple excitation space in X2C-TDDFT calculations, the X2C-MRCI approach requires more tailored partitioning of the orbital space guided by chemical considerations. These partitioning schemes are defined in a systematically improvable way by selectively allocating molecular orbitals into excitation spaces with specific excitation constraints, known as restricted active spaces (RAS), in part to manage the computational cost. We note that this should not be confused with a restricted active space self-consistent field

(RASSCF) calculation. Here, the RAS notation is used to indicate the excitations included in MRCI itself, or excitations beyond the space in which orbital optimization was performed. The molecular orbitals in an X2C-MRCI calculation are typically optimized using a complete or restricted active space self-consistent-field (CASSCF or RASSCF) procedure to capture strong correlation in the system, while the subsequent CI excitations recover dynamical correlation. The excited states from X2C-TDDFT can be effectively cross-referenced with the results obtained via configuration interaction singlet (CIS) calculations. This cross-referencing allows for the creation of active space partitioning in X2C-MRCI that is in close alignment with the X2C-TDDFT calculations, leading to a natural comparison between the two approaches.

Within the reference orbitals, two different active space partitioning schemes are proposed that systematically increase the number of configurations included in calculating the Cl Kedge spectra. For the Ce molecular complexes under study, we have selected two distinct active space partitioning schemes, denoted as Scheme A and Scheme B (see Figure 2 and the Computational Methods section for details). These schemes are strategically designed to increase complexity by incorporating a broader set of correlated orbitals and higher order excitations. Within Scheme B, two excitation restrictions are employed. Scheme B(1e) allows only a single excitation from occupied orbital space, whereas Scheme B(2e) includes up to two electron excitations. Particularly, Scheme B(2e) introduces additional electron correlation and enables studies of ligandhole coupled excitations. See the Computational Methods section for details.

By employing X2C-TDDFT and X2C-MRCI calculations with various orbital space partitioning and excitation limitations, we established a methodical framework for systematically investigating the 4f-orbital covalency in Ce complexes. This approach not only aids in the analysis itself but also deepens our understanding of how ligand-hole relaxation and electron correlation impact spectroscopic outcomes.

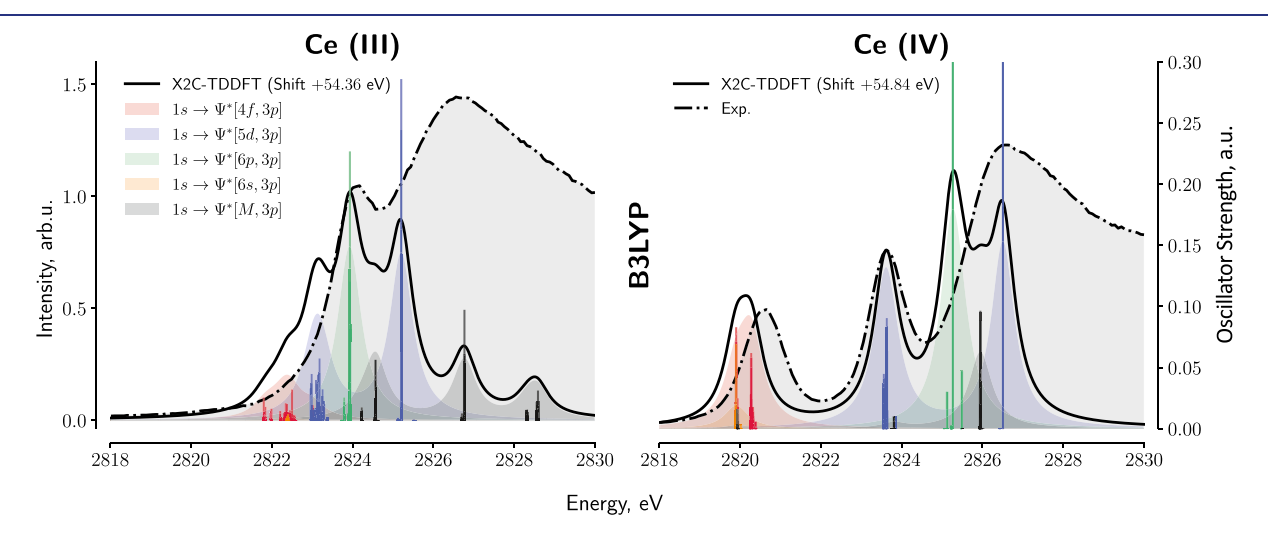


Figure 3. Cl K-edge of (left) $[Ce(III)Cl_6]^{3-}$ and (right) $[Ce(IV)Cl_6]^{2-}$, simulated with X2C-TDDFT (B3LYP). Lorentzian broadening of $\sigma = 0.7$ eV was applied to the calculated peaks to reproduce the smooth spectrum. ⁴⁸ The left y-axis shows normalized intensity in arbitrary units. The right y-axis shows absolute oscillator strengths of the transition peaks in atomic units. Experimental data are reproduced from ref 25. The spectra obtained from computations were uniformly shifted to align the peak with the highest pre-edge intensity to match that observed in the experimental data.

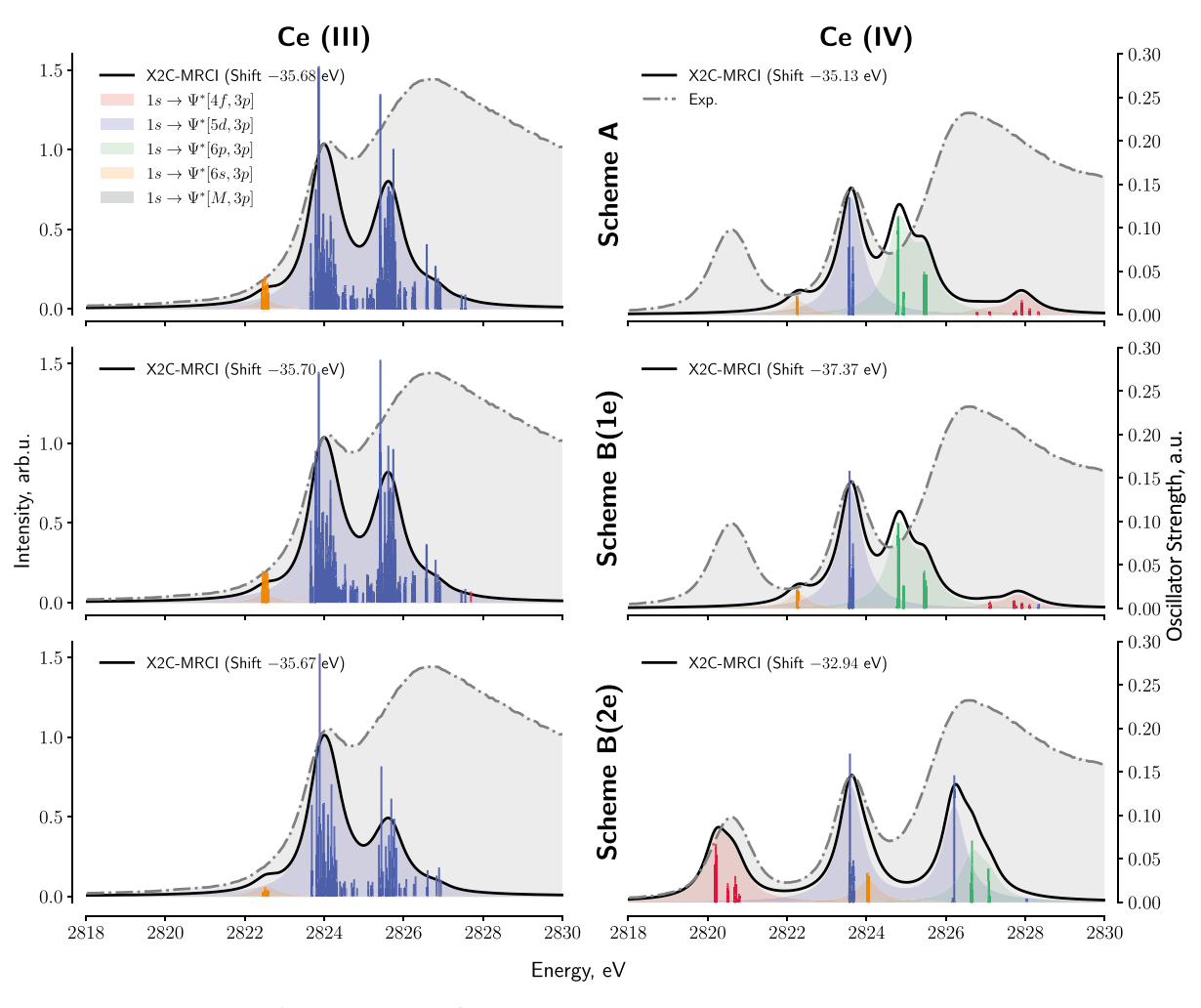


Figure 4. Cl K-edge of $[Ce(IV)Cl_6]^{4-}$ and $[Ce(III)Cl_6]^{3-}$ calculated with Scheme A, Scheme B(1e), and Scheme B(2e) X2C-MRCI schemes (Figure 2). Lorentzian broadening of $\sigma = 0.7$ eV was applied to the calculated peaks to reproduce the smooth spectrum. The left y-axis shows normalized intensity in arbitrary units, associated with the broadened spectrum. The right y-axis shows absolute oscillator strengths of the transition peaks in atomic units. Experimental data are reproduced from ref 25. The spectra obtained from computations were uniformly shifted to align the peak with the highest pre-edge intensity to match that observed in the experimental data.

3. RESULTS

3.1. Extent of 4f Covalency in X2C-TDDFT. The comparison between the Cl K-edge spectra computed using relativistic X2C-TDDFT and the experiment²⁵ is shown in Figure 3. Both Ce(III) and Ce(IV) hexachloride complexes exhibit pre-edge peaks around ~2824 eV, which can be attributed to $\text{Cl}[1s] \to \Psi^*[\text{Sd, 3p}]$ transitions. Due to the electronic transitions from Cl[1s] to empty p-type orbitals being highly dipole-allowed, the strength of these peaks is directly related to the degree of Cl[3p]-Ce[5d] orbital overlap or p/d hybridization.

Notably, the Cl K-edge spectrum for Ce(IV) hexachloride also displays a pronounced feature near $\sim\!\!2820$ eV, similar to features in ligand K-edge spectra of related Ce(IV) materials, CeO2 and [Ce(C_8H_8)_2]^2-.21,31 Population analyses (vide infra) reveal that the $\sim\!\!2820$ peak in Ce(IV) hexachloride corresponds to 1s[Cl] \to $\Psi^*[4f, 3p]$ transitions. These same transitions also exist in the X2C-TDDFT-computed Ce(III) hexachloride spectrum, albeit with significantly lower intensity and closer energy to the Cl[1s] \to $\Psi^*[5d, 3p]$ peak. Please note that the computed peak intensities were determined based on transition dipole moments, considering that

intensities arising from higher order moments (such as quadrupole, octupole, etc.) are expected to be significantly weaker compared to the dipole intensity (see Figure S2 in the Supporting Information). The most notable conclusion from X2C-TDDFT is that it predicts that excitations into a Ce(III)[4f]-Cl[3p] antibonding orbital results in a low energy shoulder peak next to the strong $Cl[1s] \rightarrow \Psi^*[5d, 3p]$ peak.

Population analysis based on X2C-DFT spinor orbitals of the Ce(IV) f⁰ ground state reveals that the Cl[3p]-Ce[4f] orbitals include on average a 6% contribution from Cl[3p], resulting in the observed strong dipole-allowed pre-edge peak. The experimentally determined value for the Cl[3p] contribution in the Ce(IV) system is ~10%.²⁵ In the case of Ce(III) hexachloride, the extent of Cl[3p]-Ce[4f] mixing is significantly reduced, with only 2% contribution from Cl[3p] based on X2C-DFT calculations, compared to an estimated \sim 1% from the experiment. ²⁵ Consequently, the intensity of the $Cl[1s] \rightarrow \Psi^*[4f, 3p]$ transition is considerably weaker in Ce(III) compared to Ce(IV). However, both current and past TDDFT calculations²⁵ reveal a prominent pre-edge in the Ce(III) molecular complex, indicative of Cl[3p]-Ce[4f] covalency, a feature that cannot be assigned definitively from the experimental spectrum. In other words, despite the ground

state analysis indicating minimal covalency within the Ce(III) molecular complex, the TDDFT-computed X-ray pre-edge spectrum displays a shoulder peak suggesting that even a small amount of orbital mixing leads to the stabilization of the 4f orbitals causing the transitions to occur at a lower energy than excitations into the 5d orbitals. This stabilization of the 4f orbitals is also present in the Ce(IV) complex. As a result, the peak spacing between the two pre-edge features is larger in X2C-TDDFT than in the experiment.

3.2. Extent of 4f Covalency in X2C-MRCI. Continuing our efforts to understand the importance of recovering both relativistic effects and electron correlation in predicting spectra accurately, we employed advanced X2C-MRCI computations to address the nuances in peak assignment and spectral spacing. Compared to X2C-TDDFT, these calculations recover strong correlation within the multireference calculation, while the MRCI partitioning schemes can be systematically expanded to recover a significant amount of dynamic correlation. The Cl K-edge pre-edge features computed using the variational X2C-MRCI method for Ce(III) and Ce(IV) hexachloride complexes are reported in Figure 4, along with comparisons to the experiment.

It is immediately clear, although not surprising, that the orbital partitioning scheme impacts the agreement with experiment. Specifically, the calculated spectra based on Scheme A and Scheme B(1e) for Ce(IV) exhibit good agreement with the experiment for the Cl[1s] $\rightarrow \Psi^*[5d, 3p]$ peak, but the Cl[1s] $\rightarrow \Psi^*[4f, 3p]$ peak is significantly blue-shifted and has a lower intensity compared to the prediction made by X2C-TDDFT. From the perspective of the electronic wave function, this result suggests that the 4f orbitals from X2C-MRCI with limited excitations, especially when these schemes restrict the ability to form a ligand-hole excitation, do not sufficiently recover dynamic correlation. As a result, the 4f orbitals are destabilized (overlocalized) compared to those predicted by X2C-TDDFT.

In order to provide a more accurate XAS prediction and directly assess these questions about orbital stabilization/ destabilization, X2C-MRCI with Scheme B(2e) was employed (Figure 4). This scheme allows for double excitation from RAS-1 and single occupancy in RAS-3. In other words, a simultaneous excitation from Cl[1s] and Cl[3p] orbitals into the $\Psi^*[4f, 3p]$ and $\Psi^*[5d, 3p]$ orbitals is permitted, capturing not only additional dynamic correlation but also ligand-hole excitations. X2C-MRCI with Scheme B(2e) produces a K-edge spectrum for Ce(IV) hexachloride that is in excellent agreement with the experiment for the first two main peaks in terms of both relative peak intensities and spacing. This agreement is improved compared to both prior literature^{25,43} and work herein using either a smaller active space and with X2C-TDDFT. The lack of specific features in the third peak is mainly due to an inadequate number of excited states resolved in this region, along with the experimental spectrum's overlap with the continuum.

Similar X2C-MRCI calculations were carried out for the Ce(III) hexachloride complex (Figure 4). In contrast to the Ce(IV) complex, the Ce(III) complex displays a spectral profile in alignment with experimental data across all the three orbital partitioning schemes utilized in the X2C-MRCI XAS computations. Notably, it does not show the lower-energy shoulder peak that appears below the main $\Psi^*[5d, 3p]$ transitions in the X2C-TDDFT analysis (Figure 3). Additionally, the X2C-MRCI calculated spectra do not show any

significant progression with increasing computational complexity from Scheme A to Scheme B(1e) and Scheme B(2e). In sharp contrast to the scalar relativistic TD-DFT and X2C-TDDFT results, there is no evidence of Ce[4f] covalency in the pre-edge region of the X2C-MRCI spectrum. Adding more dynamic correlation using Scheme B(2e) does not change the spectral characteristics, suggesting that the spectral features have reached convergence in terms of the active space. Population analysis using state-average X2C-CASSCF(1e, 14o)-optimized spinor orbitals of the Ce(III) system supports that the Ce[4f]—Cl[3p] mixing in the ground state is in the range of 0.05—1.05%. This result is in excellent agreement with the curve-fit analysis of the experimental spectrum in the original report.²⁵

4. DISCUSSION

4.1. f-Orbital Overstabilization in Density Functional Theory vs Overdestabilization with a Small Active Space. The X2C-TDDFT results demonstrate an amplification of the 4f overstabilization in DFT. In the Ce(IV) $4f^0$ complex, this overstabilization results in an overestimation of the peak splitting between the $Cl[1s] \rightarrow Ce[4f]$ peak and the $Cl[1s] \rightarrow Ce[5d]$ peak.

On the other hand, X2C-TDDFT predicts the same two peaks in the Ce(III) $4f^1$ complex, albeit with the Cl[1s] \rightarrow Ce[4f] transition at a lower intensity. However, the Cl[1s] excitation to a virtual orbital in the Ce(III) complex should give rise to an effective Ce(II) core configuration. The lowest energy excited state corresponding to a Ce(II) configuration is 4f¹5d¹ due to weaker electron-electron repulsion than the 4f² configuration, confirmed by the X2C-MRCI calculations. Specifically, the 4f² configuration of Ce(II) is 0.16 eV higher in energy than that of 4f¹5d¹. In other words, the Cl K-edge pre-edge excitation for the Ce(III) complex should correspond to $Cl[1s] \rightarrow Ce[5d]$ that results in a $4f^15d^1$ Ce electronic structure, and the $Cl[1s] \rightarrow Ce[4f]$ transition should appear in a higher energy region than the Ce[5d] manifold. All X2C-MRCI calculations correctly predicted the spectral ordering of Cl K-edge XAS of the Ce(III) complex. With these high-level X2C-MRCI calculations in hand, it is now clear that X2C-TDDFT overstabilizes the Ce[4f] orbitals in both complexes. However, in the Ce(III) system, this leads to $Cl[1s] \rightarrow Ce[4f]$ being lower in energy than the transition to the Ce[5d] manifold and an inaccurately strong representation of 4f covalency.

Returning to the Ce(IV) complex, $Cl[1s] \rightarrow Ce[4f]$ excitation gives rise to a 4f1 Ce or an effective Ce(III) core configuration. As a result, the Cl K-edge pre-edge should feature a Ψ*[4f, 3p] peak, correctly predicted by X2C-TDDFT. However, X2C-TDDFT once more overstabilizes the Ce[4f] orbital, resulting in a larger peak splitting compared to the experiment between $\Psi^*[4f, 3p]$ and $\Psi^*[5d, 3p]$ peaks in the Ce(IV) Cl K-edge XAS spectrum. In contrast, relativistic multireference methods that use a small active space [e.g., X2C-MRCI using Scheme A and Scheme B(1e)] do not recover the dynamic correlation sufficiently, which is important for f-electrons. This leads to a serious overdestabilization of the Ce[4f] orbitals. As a result, the Ce 4f¹ configuration, arising from the $Cl[1s] \rightarrow Ce[4f]$ excitation, is positioned in an incorrect energy range when Scheme A and Scheme B(1e) are used. When dynamic correlation is properly accounted for in Scheme B(2e), X2C-MRCI produces the Cl K-edge spectrum

Table 1. Contributions of Different Electrons Configuration to the Ground State of $Ce(IV)Cl_6^{4-}$ and $Ce(III)Cl_6^{3-}$ within X2C-MRCI Formalism

scheme	Ce(III)			Ce(IV)				
	$\ket{\mathrm{f^1}}$ (%)	$ \underline{L}f^{i}d^{i}\rangle$ (%)	$ \underline{\mathrm{L}}\mathrm{f}^2\rangle$ (%)	$ \mathrm{f}^0 angle~(\%)$	$\ket{\underline{L} f^1}$ (%)	$ \underline{L}d^{1}\rangle$ (%)	$ \underline{L}^2f^ld^l\rangle$ (%)	$ \underline{L}^2f^2\rangle$ (%)
A B(1e) B(2e)	100.00 99.92 99.85	0.00 0.04 0.04	0.00 0.01 0.02	100.0 91.39 90.74	0.00 8.41 8.57	0.00 0.02 0.06	0.00 0.00 0.56	0.00 0.00 0.08

for the Ce(IV) complex in excellent agreement with the experiment, both in terms of peak separation and assignment.

4.2. Nature of the Ground State and the Role of Ligand-Hole Configurations. The two Ce complexes exhibited rather different spectral progressions as the active space and the level of dynamic correlation were increased in the X2C-MRCI calculations, Scheme B(2e). This difference is a direct consequence of the fact that in 4f complexes, strong correlation, dynamic correlation, relativistic effects, and ligand-hole configurations should be accounted for in a balanced way. Particularly, the ligand-hole configuration ($\underline{\mathbf{L}}$) plays an important role in the 4f electronic structure.

Specifically, X2C-MRCI calculations show that the ground state of the Ce(III) complex is dominated by the f^1 configuration with less than 0.1% contribution from the ligand-hole configuration ($\underline{L}f^1d^1$) for all three Schemes (Table 1). In other words, the electronic structure of the ground state of the Ce(III) complex can be sufficiently described by a single configuration and the Cl K-edge excitation by a one-electron excitation operator. Recall that the transition occurs from Cl[1s] to Ce[5d] in the Ce(III) complex due to the preference of the excited state to adopt a Ce(II) core with a $4f^15d^1$ configuration. As a result, no peak associated with an excitation into a 4f orbital is observed, and the computed spectra exhibit minimal progression in spectral characteristics as the correlation space increases.

In contrast, relativistic multireference calculations reveal that the Ce(IV) complex has more multiconfigurational character in the ground state. The percentages of closed-shell $4f^0$ and ligand-hole $\underline{L}f^1$ configurations in the ground state of the Ce(IV) molecular complex are given in Table 1. With the exception of Scheme A, the f^0 configuration comprises ~91% of the ground state, while the $\underline{L}f^1$ configuration contributes ~8.5%. One would generally assign ground-state CASSCF wave functions in which one state contributes 91% as single reference and, in turn, may expect that DFT should be able to recover this percentage of multiconfigurational character. The results herein show that this threshold cannot be so easily extended to XAS spectra even for complexes where the metalligand bond is predominately electrostatic.

What does the ground state multiconfigurational character mean in the context of 4f stability? The results for the Ce(IV) system suggest that in the reference DFT orbitals, the electron density tends to be overlocalized between the bonds, and in a minimal active space (Scheme A), this bias remains since excitations out of the occupied 3p orbitals are not permitted. When such an excitation is allowed, the electron density can correct for this overlocalization along the bond. This is an example of left—right correlation, ⁴⁹ where including excitations from bonding orbitals allows the charge density to be redistributed along the chemical bonds correcting for this

overlocalization. The ground state ligand-hole configuration also provides further evidence of Cl[3p]—Ce[4f] covalency. The Cl K-edge XAS spectra are sensitive to the correlation effect from the ligand-hole configurations and allow one to quantify the importance of this effect.

Interestingly, even though Ce(IV) displays a more multiconfigurational nature than Ce(III), single-reference-based X2C-TDDFT performs more accurately for Ce(IV) than for Ce(III). It is important to point out that in the ground state of Ce(IV), the predominant configuration is f⁰ (no occupied f orbitals). Consequently, the issue of f electron overstabilization is significantly mitigated in DFT calculations, making dynamic correlation the primary error source.

An important consequence of the multireference character of the Ce(IV) hexachloride ground state is that subsequent electronic excitations are strongly correlated. As a result, electronic structure methods for correctly predicting XAS spectra must include an accurate correlation treatment. This strong correlation of electronic excitations explains why the Cl K-edge spectrum for the Ce(IV) complex is strongly dependent on the correlation space and the level of electron excitations in the X2C-MRCI calculations, while the spectrum of the Ce(III) complex does not have such a dependence.

5. CONCLUSIONS AND PERSPECTIVES

This work analyses 4f-orbital mixing as manifested in the Cl K-edge XAS spectra of the $[\mathrm{Ce}(\mathrm{III})\mathrm{Cl}_6]^{3-}$ and $[\mathrm{Ce}(\mathrm{IV})\mathrm{Cl}_6]^{2-}$ complexes. These experiments and associated computations have been crucial in developing a more nuanced language around covalency in the f-element community. Herein, advanced variational relativistic electronic structure methods were applied to characterize not only the spectroscopic signatures of $\mathrm{Ce}[4f]\mathrm{-Cl}[3p]$ covalency in spectra of these complexes but also the importance of the ligand-hole configuration in the ground state wave function.

Computed spectra suggest that density functional theory can overstabilize 4f orbitals leading to erroneous covalency assessments. On the other hand, small active space calculations can result in an equally erroneous assessment but the opposite in nature, an overdestabilization of the 4f orbitals. Relativistic multireference calculations also revealed an apparent "multiconfigurational" character in the ground state of the Ce(IV) complex, best described as left—right correlation, with a significant contribution from the ligand-hole configuration.

Results from this study highlight the critical importance of using large active space, multireference, and relativistic electronic structure methods for examining f-block complexes. Additionally, researchers should exercise caution when utilizing low-scaling electronic structure methods in computational analyses of rare earth and lanthanide complexes. Such approaches could produce misleading results, potentially leading to an incorrect interpretation of the complex chemical

bonding inherent in the f-elements. On the other hand, XAS spectra of f-block elements offer a unique avenue for advancing density functional theory, a cornerstone of modern computational chemistry. This presents an opportunity to develop new exchange-correlation kernels that can simultaneously address both relativistic effects and dynamic correlation. Additionally, the physical insights learned by "turning on" and "turning off" participating orbitals and excitations can aid in building robust multiplet models that take into account scalar relativity, spinorbit, strong and dynamic correlation, as well as the ligand-hole effect. In the analysis of these benchmark Cl K-edge spectra of the $[Ce(III)Cl_6]^{3-}$ and $[Ce(IV)Cl_6]^{2-}$ complexes, the methodology described here realizes a substantially improved model of the experimentally observed spectra. Importantly, the study recovers a model of metal-ligand bonding in trivalent lanthanide complexes, with less than 1% Ce[4f]-Cl[3p] mixing in the ground state of [Ce(III)Cl₆]³⁻, that is congruent with prior optical spectroscopic studies.

6. COMPUTATIONAL METHODS

All calculations in this work have been performed with the Gaussian software package (development version), 50 using the X2C-TZVPPall-2c all-electron basis set.⁵¹ Geometries of both structures of [CeCl₆]ⁿ (n = 2 and 3) have been optimized using the unrestricted B3LYP hybrid functional^{52,53} with the scalar relativistic effects, treated via scalar-X2C approach. The initial geometry before optimization was assumed to be an ideal octahedral (O_h) with bond lengths equal to the one determined experimentally [2.599 Å for Ce(IV) and 2.770 Å for Ce(III)]. The bond lengths after the optimization were 2.681 and 2.876 Å. The independence of spectra with respect to geometry was tested and confirmed. A single initial octahedral geometry of $[Ce(IV)Cl_{\delta}]^{3-}$ has been taken and altered to deviate from ideal $O_{l_{\delta}}$ to include some positional Gaussian noise with mean in around experimental bond length and standard deviation equal to experimental uncertainty. Five structures have been generated this way, optimized with X2C-DFT without the imposition of symmetry constraints. All five structures yielded similar Cl K-edge XAS spectra under the X2C-MRCI formalism.

For electronic structure calculations of XAS, the one-electron exact-two-component (X2C) Hamiltonian, $^{46,54-73}$ including scalar relativity and one-electron spin-orbit coupling, is used in all-electron X2C-TDDFT and X2C-MRCI. The screened-nuclear spin-orbit approach^{74,75} is used with the one-electron spin-orbit term to take into account the two-electron spin-orbit effects. All calculations are performed using Kramers' unrestricted formalism.

Cl K-edge XANES spectra of the $[Ce(III)Cl_6]^{3-}$ and $[Ce(IV)Cl_6]^{2-}$ complexes have been simulated using the relativistic X2C-TDDFT⁴⁶ approach with the B3LYP exchange-correlation functional. Additional X2C-TDDFT calculations using different exchange-correlation functionals can be found in the Supporting Information. Excited states were converged using the energy specific 6-78 Davidson algorithm to 10⁻⁸ au on excitation amplitudes of the desired states. Transition dipole moments and transition amplitudes were calculated between ground and excited states. To account for core-hole relaxation and errors embedded in the DFT functional, a uniform shift (indicated in the figures) has been applied to the XAS spectra, such that calculated peaks, associated with $Cl[1s] \rightarrow \Psi^*[5d, 3p]$ orbital excitations, are aligned with experimental spectra.

X2C-MRCI calculations 47,79,80 have been performed on both anions to simulate Cl K-edge XAS spectra. Prior to X2C-MRCI calculations, for the [Ce(III)Cl₆]³⁻ anion, state-average X2C-CASSCF⁷⁹ over the lowest 14 states was used to optimize the reference orbitals. The optimized reference orbitals are then mapped on to RAS spaces for the X2C-MRCI calculations to obtain the XAS spectra. For the closed-shell [Ce(IV)Cl₆]²⁻ anion, analogous X2C-CASSCF calculations cannot be performed; therefore, DFT-X2C

orbitals are taken as the reference. Excited states were converged using the energy specific Davidson algorithm with 10^{-8} convergence criteria on the excitation amplitudes of desired states.

Considering atomic orbitals, Scheme A includes 12 Cl[1s] orbitals in RAS-1, 14 Ce[4f] orbitals in RAS-2, and 10 Ce[5d] orbitals in RAS-3, as shown in Figure 2. Note that the calculations are performed in a Kramers' unrestricted two-component formalism, using a spinor basis where each orbital contains only one electron. As a result, the number of orbitals in the active space is two times larger than that of the corresponding nonrelativistic formalism. This can be denoted (12e, 1h, 1e; 12o, 14o, and 18o) in the notation proposed by Sauri et al.81 indicating the total number of electrons in the active space, the total holes in RAS-1, and the total electrons in RAS-3, followed by the number of spinors in the three subspaces (see Table 2). K-edge pre-

Table 2. X2C-MRCI Schemes for Ce (IV) and Ce (III) Systems used in This Work^a

scheme	standard notation	system
CAS	(1e; 14o)	Ce(III)
A	(12e, 1h, 1e; 12o, 14o, 18o)	Ce(IV)
	(13e, 1h, 1e; 12o, 14o, 18o)	Ce(III)
B(1e)	(48e, 1h, 1e; 48o, 14o, 18o)	Ce(IV)
	(49e, 1h, 1e; 48o, 14o, 18o)	Ce(III)
B(2e)	(48e, 2h, 1e; 48o, 14o, 18o)	Ce(IV)
	(49e, 2h, 1e; 48o, 14o, 18o)	Ce(III)

 a The RAS spaces in standard notations are labeled as $(n_e, n_h, n_p; n_1,$ $(n_2, n_3)^{81}$ where, (n_1, n_2) and (n_3) are the number of spinors in the RAS 1, RAS 2, and RAS 3, respectively, n_e is the total number of electrons in the active space, $n_{\rm h}$ is the maximum number of holes allowed in RAS 1, and n_p is the maximum number of electrons in RAS 3.

edge spectra, corresponding to electron excitations from RAS-1 to either RAS-2 (Ψ *[4f, 3p]) or RAS-3 (Ψ *[5d, 3p] + Ψ *[6p, 3p] + $\Psi^*[6s, 3p]$) can be captured by Scheme A. However, this scheme is limited in that it offers only a qualitative description of electron excitations as it does not allow for ligand-hole relaxation and recovers less dynamic correlation. On the other hand, Scheme B includes the Cl[1s] orbitals and all ligand Cl[3p] orbitals in RAS-1 with the aim of accounting for ligand-hole relaxation for a total of 18 orbitals. Once more, the active space in the spinor basis including single excitations within the RAS spaces is denoted as Scheme B(1e), (48e, 2h, 2e; 48o, 140, 180). To capture additional dynamic correlation in the XAS calculations, the incorporation of double-electron excitations from the RAS-1 space becomes necessary. This enlarges the determinant space for the X2C-MRCI calculations to (48e, 2h, 2e; 48o, 14o, and 18o) but results in greater accuracy [Scheme B(2e)]. Note that single excitations in MRCI are not equivalent to configuration interaction singles (CIS) because there is no excitation restriction in the RAS-2 space which can lead to higher-order excitations.

ASSOCIATED CONTENT

Solution Supporting Information

The Supporting Information is available free of charge at https://pubs.acs.org/doi/10.1021/jacs.4c01665.

Additional X2C-TDDFT calculations using different exchange-correlation functionals, spectrum of Ce(III) including electric-dipole contributions, and spectrum of Ce(IV) using a much larger RAS3 space (PDF)

AUTHOR INFORMATION

Corresponding Authors

Henry S. La Pierre – School of Chemistry and Biochemistry and Nuclear and Radiological Engineering and Medical Physics Program, School of Mechanical Engineering, Georgia Institute of Technology, Atlanta, Georgia 30332, United

States; Physical Sciences Division, Pacific Northwest National Laboratory, Richland, Washington 99352, United States; orcid.org/0000-0002-0895-0655; Email: la_pierre@chemistry.gatech.edu

Bess Vlaisavljevich — Department of Chemistry, University of South Dakota, Vermillion, South Dakota 57069, United States; orcid.org/0000-0001-6065-0732; Email: Bess.Vlaisavljevich@usd.edu

Xiaosong Li — Department of Chemistry, University of Washington, Seattle, Washington 98195, United States; orcid.org/0000-0001-7341-6240; Email: xsli@uw.edu

Authors

Kirill D. Shumilov — Department of Chemistry, University of Washington, Seattle, Washington 98195, United States

Andrew J. Jenkins — Department of Chemistry, University of Washington, Seattle, Washington 98195, United States;

orcid.org/0000-0002-1014-5225

Complete contact information is available at: https://pubs.acs.org/10.1021/jacs.4c01665

Notes

The authors declare no competing financial interest.

ACKNOWLEDGMENTS

Studies of the lanthanide electronic structure is supported by the U.S. Department of Energy, Office of Science, Basic Energy Sciences, under the Quantum Information Science initiative (Grant no. DE-SC0023455). Computations were facilitated through the use of advanced computational, storage, and networking infrastructure provided by the shared facility supported by the University of Washington Molecular Engineering Materials Center (DMR-2308979) via the Hyak supercomputer system. B.V. was supported by the U.S. Department of Energy, Office of Science, Basic Energy Sciences, in the Heavy-Element Chemistry program (Grant no. DE-SC0023022).

REFERENCES

- (1) Cheisson, T.; Schelter, E. J. Rare Earth Elements: Mendeleev's Bane, Modern Marvels. *Science* **2019**, *363*, 489–493.
- (2) Humphries, M. Rare Earth Elements: The Global Supply Chain; U.S. Congressional Research Service, 2013.
- (3) Lanthanides and Actinides in Molecular Magnetism, 1st ed.; Layfield, R. A., Murugesu, M., Eds.; Wiley, 2015.
- (4) Aguilà, D.; Barrios, L. A.; Velasco, V.; Roubeau, O.; Repollés, A.; Alonso, P. J.; Sesé, J.; Teat, S. J.; Luis, F.; Aromí, G. Heterodimetallic [LnLn'] Lanthanide Complexes: Toward a Chemical Design of Two-Qubit Molecular Spin Quantum Gates. *J. Am. Chem. Soc.* **2014**, *136*, 14215–14222.
- (5) Aromí, G.; Luis, F.; Roubeau, O. Lanthanides and Actinides in Molecular Magnetism; John Wiley & Sons, Ltd, 2015; Chapter 7, pp 185–222.
- (6) Ding, Y.-S.; Deng, Y.-F.; Zheng, Y.-Z. The Rise of Single-Ion Magnets as Spin Qubits. *Magnetochemistry* **2016**, 2, 40.
- (7) Luis, F.; Repollés, A.; Martínez-Pérez, M. J.; Aguilà, D.; Roubeau, O.; Zueco, D.; Alonso, P. J.; Evangelisti, M.; Camón, A.; Sesé, J.; Barrios, L. A.; Aromí, G. Molecular Prototypes for Spin-Based CNOT and SWAP Quantum Gates. *Phys. Rev. Lett.* **2011**, *107*, 117203.
- (8) Leskelä, M. Rare Earths in Electroluminescent and Field Emission Display Phosphors. *J. Alloys Compd.* **1998**, 275–277, 702–708.
- (9) Nehra, K.; Dalal, A.; Hooda, A.; Bhagwan, S.; Saini, R. K.; Mari, B.; Kumar, S.; Singh, D. Lanthanides β -diketonate complexes as

- energy-efficient emissive materials: A review. J. Mol. Struct. 2022, 1249, 131531.
- (10) Pressler, K.; Snoeren, T. J.; Walsh, K. M.; Gamelin, D. R. Magnetic Amplification at Yb³⁺ "Designer Defects" in the van Der Waals Ferromagnet CrI₂. Nano Lett. **2023**, 23, 1320–1326.
- (11) Milstein, T. J.; Kroupa, D. M.; Gamelin, D. R. Picosecond Quantum Cutting Generates Photoluminescence Quantum Yields Over 100% in Ytterbium-Doped CsPbCl₃ Nanocrystals. *Nano Lett.* **2018**, *18*, 3792–3799.
- (12) Yao, J.-S.; Ge, J.; Han, B.-N.; Wang, K.-H.; Yao, H.-B.; Yu, H.-L.; Li, J.-H.; Zhu, B.-S.; Song, J.-Z.; Chen, C.; Zhang, Q.; Zeng, H.-B.; Luo, Y.; Yu, S.-H. Ce³⁺-Doping to Modulate Photoluminescence Kinetics for Efficient CsPbBr₃ Nanocrystals Based Light-Emitting Diodes. *J. Am. Chem. Soc.* **2018**, *140*, 3626–3634.
- (13) Zhou, D.; Liu, D.; Pan, G.; Chen, X.; Li, D.; Xu, W.; Bai, X.; Song, H. Cerium and Ytterbium Codoped Halide Perovskite Quantum Dots: A Novel and Efficient Downconverter for Improving the Performance of Silicon Solar Cells. *Adv. Mater.* **2017**, 29, 1704149
- (14) The Chemistry of the Actinide Elements, 2nd ed.; Katz, J. J., Seaborg, G. T., Morss, L. R., Eds.; Chapman and Hall: London; New York, 1986.
- (15) Singh, S. K.; Eng, J.; Atanasov, M.; Neese, F. Covalency and Chemical Bonding in Transition Metal Complexes: An Ab Initio Based Ligand Field Perspective. *Coord. Chem. Rev.* **2017**, 344, 2–25.
- (16) Neidig, M. L.; Clark, D. L.; Martin, R. L. Covalency in F-Element Complexes. *Coord. Chem. Rev.* **2013**, 257, 394–406.
- (17) Bünzli, J. C. G.; Piguet, C. Taking Advantage of Luminescent Lanthanide Ions. *Chem. Soc. Rev.* **2005**, *34*, 1048–1077.
- (18) Crosswhite, H. M.; Crosswhite, H.; Carnall, W. T.; Paszek, A. P. Spectrum Analysis of U³⁺:LaCl₃. *J. Chem. Phys.* **1980**, 72, 5103–5117.
- (19) Liddle, S. T. The Renaissance of Non-Aqueous Uranium Chemistry. *Angew. Chem., Int. Ed.* **2015**, *54*, 8604–8641.
- (20) Altman, A. B.; Pacold, J. I.; Wang, J.; Lukens, W. W.; Minasian, S. G. Evidence for $Sd-\sigma$ and $Sd-\pi$ Covalency in Lanthanide Sesquioxides from Oxygen K-edge X-ray Absorption Spectroscopy. *Dalton Trans.* **2016**, *45*, 9948–9961.
- (21) Minasian, S. G.; Batista, E. R.; Booth, C. H.; Clark, D. L.; Keith, J. M.; Kozimor, S. A.; Lukens, W. W.; Martin, R. L.; Shuh, D. K.; Stieber, S. C. E.; Tylisczcak, T.; Wen, X.-d. Quantitative Evidence for Lanthanide-Oxygen Orbital Mixing in CeO₂, PrO₂, and TbO₂. *J. Am. Chem. Soc.* **2017**, *139*, 18052–18064.
- (22) Lukens, W. W.; Minasian, S. G.; Booth, C. H. Strengths of Covalent Bonds in LnO₂ Determined from O K-edge XANES Spectra Using a Hubbard Model. *Chem. Sci.* **2023**, *14*, 12784–12795.
- (23) Ramanathan, A.; Kaplan, J.; Sergentu, D.-C.; Branson, J. A.; Ozerov, M.; Kolesnikov, A. I.; Minasian, S. G.; Autschbach, J.; Freeland, J. W.; Jiang, Z.; Mourigal, M.; La Pierre, H. S. Chemical Design of Electronic and Magnetic Energy Scales of Tetravalent Praseodymium Materials. *Nat. Commun.* **2023**, *14*, 3134.
- (24) Jung, J.; Atanasov, M.; Neese, F. Ab Initio Ligand-Field Theory Analysis and Covalency Trends in Actinide and Lanthanide Free Ions and Octahedral Complexes. *Inorg. Chem.* **2017**, *56*, 8802–8816.
- (25) Löble, M. W.; Keith, J. M.; Altman, A. B.; Stieber, S. C. E.; Batista, E. R.; Boland, K. S.; Conradson, S. D.; Clark, D. L.; Lezama Pacheco, J.; Kozimor, S. A.; Martin, R. L.; Minasian, S. G.; Olson, A. C.; Scott, B. L.; Shuh, D. K.; Tyliszczak, T.; Wilkerson, M. P.; Zehnder, R. A. Covalency in Lanthanides. An X-ray Absorption Spectroscopy and Density Functional Theory Study of $LnCl_6^{x-}$ (x = 3, 2). *J. Am. Chem. Soc.* **2015**, *137*, 2506–2523.
- (26) Cross, J. N.; Su, J.; Batista, E. R.; Cary, S. K.; Evans, W. J.; Kozimor, S. A.; Mocko, V.; Scott, B. L.; Stein, B. W.; Windorff, C. J.; Yang, P. Covalency in Americium(III) Hexachloride. *J. Am. Chem. Soc.* 2017, 139, 8667–8677.
- (27) Dumas, T.; Guillaumont, D.; Fillaux, C.; Scheinost, A.; Moisy, P.; Petit, S.; Shuh, D. K.; Tyliszczak, T.; Auwer, C. D. The Nature of Chemical Bonding in Actinide and Lanthanide Ferrocyanides

- Determined by X-ray Absorption Spectroscopy and Density Functional Theory. *Phys. Chem. Chem. Phys.* **2016**, *18*, 2887–2895.
- (28) Eisenstein, O.; Maron, L. DFT Studies of Some Structures and Reactions of Lanthanides Complexes. *J. Org. Chem.* **2002**, *647*, 190–197
- (29) Gompa, T. P.; Greer, S. M.; Rice, N. T.; Jiang, N.; Telser, J.; Ozarowski, A.; Stein, B. W.; La Pierre, H. S. High-Frequency and -Field Electron Paramagnetic Resonance Spectroscopic Analysis of Metal-Ligand Covalency in a 4f⁷ Valence Series (Eu²⁺, Gd³⁺, and Tb⁴⁺). *Inorg. Chem.* **2021**, *60*, 9064–9073.
- (30) Chen, Z.; Yang, J. Bonding Properties of Molecular Cerium Oxides Tuned by the 4f-Block from Ab Initio Perspective. *J. Chem. Phys.* **2022**, *156*, 211101.
- (31) Smiles, D. E.; Batista, E. R.; Booth, C. H.; Clark, D. L.; Keith, J. M.; Kozimor, S. A.; Martin, R. L.; Minasian, S. G.; Shuh, D. K.; Stieber, S. C. E.; Tyliszczak, T. The Duality of Electron Localization and Covalency in Lanthanide and Actinide Metallocenes. *Chem. Sci.* **2020**, *11*, 2796–2809.
- (32) Solomon, E. I.; Hedman, B.; Hodgson, K. O.; Dey, A.; Szilagyi, R. K. Ligand K-edge X-ray Absorption Spectroscopy: Covalency of Ligand—Metal Bonds. *Coord. Chem. Rev.* **2005**, 249, 97–129.
- (33) Shadle, S. E.; Hedman, B.; Hodgson, K. O.; Solomon, E. I. Ligand K-edge x-Ray Absorption Spectroscopic Studies: Metal-Ligand Covalency in a Series of Transition Metal Tetrachlorides. *J. Am. Chem. Soc.* **1995**, *117*, 2259–2272.
- (34) Glaser, T.; Hedman, B.; Hodgson, K. O.; Solomon, E. I. Ligand K-Edge X-ray Absorption Spectroscopy: A Direct Probe of Ligand—Metal Covalency. *Acc. Chem. Res.* **2000**, *33*, 859–868.
- (35) Hedman, B.; Hodgson, K. O.; Solomon, E. I. X-Ray Absorption Edge Spectroscopy of Ligands Bound to Open-Shell Metal Ions: Chlorine K-edge Studies of Covalency in Tetrachlorocuprate(2-). *J. Am. Chem. Soc.* **1990**, *112*, 1643–1645.
- (36) DeBeer George, S.; Neese, F. Calibration of Scalar Relativistic Density Functional Theory for the Calculation of Sulfur K-Edge X-ray Absorption Spectra. *Inorg. Chem.* **2010**, *49*, 1849–1853.
- (37) Kasper, J. M.; Lestrange, P. J.; Stetina, T. F.; Li, X. Modeling $L_{2,3}$ -Edge X-ray Absorption Spectroscopy with Real-Time Exact Two-Component Relativistic Time-Dependent Density Functional Theory. *J. Chem. Theory Comput.* **2018**, *14*, 1998–2006.
- (38) Stetina, T. F.; Kasper, J. M.; Li, X. Modeling L_{2/3}-Edge X-ray Absorption Spectroscopy with Linear Response Exact Two-Component Relativistic Time-Dependent Density Functional Theory. *J. Chem. Phys.* **2019**, *150*, 234103.
- (39) Kasper, J. M.; Stetina, T. F.; Jenkins, A. J.; Li, X. Ab Initio Methods for L-edge X-ray Absorption Spectroscopy. *Chem. Phys. Rev.* **2020**, *1*, 011304.
- (40) Kasper, J. M.; Li, X.; Kozimor, S. A.; Batista, E. R.; Yang, P. Relativistic Effects in Modeling the Ligand K-Edge X-ray Absorption Near-Edge Structure of Uranium Complexes. *J. Chem. Theory Comput.* **2022**, *18*, 2171–2179.
- (41) Sergentu, D.-C.; Autschbach, J. Covalency in Actinide (IV) Hexachlorides in Relation to the Chlorine K-edge X-ray Absorption Structure. *Chem. Sci.* **2022**, *13*, 3194–3207.
- (42) Zasimov, P.; Amidani, L.; Retegan, M.; Walter, O.; Caciuffo, R.; Kvashnina, K. O. HERFD-XANES and RIXS Study on the Electronic Structure of Trivalent Lanthanides across a Series of Isostructural Compounds. *Inorg. Chem.* **2022**, *61*, 1817–1830.
- (43) Sergentu, D.-C.; Duignan, T. J.; Autschbach, J. Ab Initio Study of Covalency in the Ground versus Core-Excited States and X-ray Absorption Spectra of Actinide Complexes. *J. Phys. Chem. Lett.* **2018**, 9, 5583–5591.
- (44) Su, J.; Batista, E. R.; Boland, K. S.; Bone, S. E.; Bradley, J. A.; Cary, S. K.; Clark, D. L.; Conradson, S. D.; Ditter, A. S.; Kaltsoyannis, N.; Keith, J. M.; Kerridge, A.; Kozimor, S. A.; Löble, M. W.; Martin, R. L.; Minasian, S. G.; Mocko, V.; La Pierre, H. S.; Seidler, G. T.; Shuh, D. K.; Wilkerson, M. P.; Wolfsberg, L. E.; Yang, P. Energy-Degeneracy-Driven Covalency in Actinide Bonding. *J. Am. Chem. Soc.* 2018, 140, 17977–17984.

- (45) Gagliardi, L. The Study of Actinide Chemistry with Multiconfigurational Quantum Chemical Methods. *Int. J. Quantum Chem.* **2011**, *111*, 3302–3306.
- (46) Egidi, F.; Sun, S.; Goings, J. J.; Scalmani, G.; Frisch, M. J.; Li, X. Two-Component Non-Collinear Time-Dependent Spin Density Functional Theory for Excited State Calculations. *J. Chem. Theory Comput.* **2017**, *13*, 2591–2603.
- (47) Jenkins, A. J.; Hu, H.; Lu, L.; Frisch, M. J.; Li, X. Two-Component Multireference Restricted Active Space Configuration Interaction for the Computation of L-Edge X-ray Absorption Spectra. *J. Chem. Theory Comput.* **2022**, *18*, 141–150.
- (48) Campbell, J. L.; Papp, T. Widths of the Atomic K-N7 Levels. At. Data Nucl. Data Tables 2001, 77, 1-56.
- (49) Handy, N. C.; Cohen, A. J. Left-Right Correlation Energy. *Mol. Phys.* **2001**, *99*, 403–412.
- (50) Frisch, M. J.; Trucks, G. W.; Schlegel, H. B.; Scuseria, G. E.; Robb, M. A.; Cheeseman, J. R.; Scalmani, G.; Barone, V.; Petersson, G. A.; Nakatsuji, H.; Li, X.; Marenich, A. V.; Caricato, M.; Bloino, J.; Janesko, B. G.; Zheng, J.; Gomperts, R.; Mennucci, B.; Hratchian, H. P.; Ortiz, J. V.; Izmaylov, A. F.; Sonnenberg, J. L.; Williams-Young, D.; Ding, F.; Lipparini, F.; Egidi, F.; Goings, J.; Peng, B.; Petrone, A.; Henderson, T.; Ranasinghe, D.; Zakrzewski, V. G.; Gao, J.; Rega, N.; Zheng, G.; Liang, W.; Hada, M.; Ehara, M.; Toyota, K.; Fukuda, R.; Hasegawa, J.; Ishida, M.; Nakajima, T.; Honda, Y.; Kitao, O.; Nakai, H.; Vreven, T.; Throssell, K.; Montgomery, J. A., Jr.; Peralta, J. E.; Ogliaro, F.; Bearpark, M. J.; Heyd, J. J.; Brothers, E. N.; Kudin, K. N.; Staroverov, V. N.; Keith, T. A.; Kobayashi, R.; Normand, J.; Raghavachari, K.; Rendell, A. P.; Burant, J. C.; Iyengar, S. S.; Tomasi, J.; Cossi, M.; Millam, J. M.; Klene, M.; Adamo, C.; Cammi, R.; Ochterski, J. W.; Martin, R. L.; Morokuma, K.; Farkas, O.; Foresman, J. B.; Fox, D. J. Gaussian Development, Version Revision
- (51) Pollak, P.; Weigend, F. Segmented Contracted Error-Consistent Basis Sets of Double- and Triple- ζ Valence Quality for One- and Two-Component Relativistic All-Electron Calculations. *J. Chem. Theory Comput.* **2017**, *13*, 3696–3705.
- (52) Lee, C.; Yang, W.; Parr, R. G. Development of the Colle-Salvetti Correlation-Energy Formula into a Functional of the Electron Density. *Phys. Rev. B* **1988**, *37*, 785–789.
- (53) Becke, A. D. Density-functional Thermochemistry. III. The Role of Exact Exchange. J. Chem. Phys. 1993, 98, 5648-5652.
- (54) Dyall, K. G. Interfacing Relativistic and Nonrelativistic Methods. I. Normalized Elimination of the Small Component in the Modified Dirac Equation. *J. Chem. Phys.* **1997**, *106*, 9618–9626.
- (55) Dyall, K. G. Interfacing Relativistic and Nonrelativistic Methods. II. Investigation of a Low-Order Approximation. *J. Chem. Phys.* **1998**, *109*, 4201–4208.
- (56) Dyall, K. G.; Enevoldsen, T. Interfacing Relativistic and Nonrelativistic Methods. III. Atomic 4-Spinor Expansions and Integral Approximations. *J. Chem. Phys.* **1999**, *111*, 10000–10007.
- (57) Dyall, K. G. Interfacing relativistic and nonrelativistic methods. IV. One- and two-electron scalar approximations. *J. Chem. Phys.* **2001**, *115*, 9136–9143.
- (58) Filatov, M.; Cremer, D. A New Quasi-Relativistic Approach for Density Functional Theory Based on the Normalized Elimination of the Small Component. *Chem. Phys. Lett.* **2002**, *351*, 259–266.
- (59) Kutzelnigg, W.; Liu, W. Quasirelativistic Theory Equivalent to Fully Relativistic Theory. *J. Chem. Phys.* **2005**, *123*, 241102.
- (60) Liu, W.; Peng, D. Infinite-Order Quasirelativistic Density Functional Method Based on the Exact Matrix Quasirelativistic Theory. *J. Chem. Phys.* **2006**, *125*, 044102.
- (61) Peng, D.; Liu, W.; Xiao, Y.; Cheng, L. Making Four- and Two-Component Relativistic Density Functional Methods Fully Equivalent Based on the Idea of from Atoms to Molecule. *J. Chem. Phys.* **2007**, 127. 104106.
- (62) Iliaš, M.; Saue, T. An Infinite-Order Two-Component Relativistic Hamiltonian by a Simple One-Step Transformation. *J. Chem. Phys.* **2007**, *126*, 064102.

- (63) Liu, W.; Peng, D. Exact Two-Component Hamiltonians Revisited. J. Chem. Phys. 2009, 131, 031104.
- (64) Liu, W. Ideas of Relativistic Quantum Chemistry. Mol. Phys. 2010, 108, 1679–1706.
- (65) Li, Z.; Xiao, Y.; Liu, W. On the Spin Separation of Algebraic Two-Component Relativistic Hamiltonians. *J. Chem. Phys.* **2012**, *137*, 154114.
- (66) Peng, D.; Middendorf, N.; Weigend, F.; Reiher, M. An Efficient Implementation of Two-Component Relativistic Exact-Decoupling Methods for Large Molecules. *J. Chem. Phys.* **2013**, *138*, 184105.
- (67) Egidi, F.; Goings, J. J.; Frisch, M. J.; Li, X. Direct Atomic-Orbital-Based Relativistic Two-Component Linear Response Method for Calculating Excited-State Fine Structures. *J. Chem. Theory Comput.* **2016**, *12*, 3711–3718.
- (68) Goings, J. J.; Kasper, J. M.; Egidi, F.; Sun, S.; Li, X. Real Time Propagation of the Exact Two Component Time-Dependent Density Functional Theory. *J. Chem. Phys.* **2016**, *145*, 104107.
- (69) Konecny, L.; Kadek, M.; Komorovsky, S.; Malkina, O. L.; Ruud, K.; Repisky, M. Acceleration of Relativistic Electron Dynamics by Means of X2C Transformation: Application to the Calculation of Nonlinear Optical Properties. *J. Chem. Theory Comput.* **2016**, *12*, 5823–5833.
- (70) Liu, J.; Cheng, L. Relativistic Coupled-Cluster and Equation-of-Motion Coupled-Cluster Methods. *Wiley Interdiscip. Rev.: Comput. Mol. Sci.* **2021**, *11*, No. e1536.
- (71) Sharma, P.; Jenkins, A. J.; Scalmani, G.; Frisch, M. J.; Truhlar, D. G.; Gagliardi, L.; Li, X. Exact-Two-Component Multiconfiguration Pair-Density Functional Theory. *J. Chem. Theory Comput.* **2022**, *18*, 2947–2954.
- (72) Lu, L.; Hu, H.; Jenkins, A. J.; Li, X. Exact-Two-Component Relativistic Multireference Second-Order Perturbation Theory. *J. Chem. Theory Comput.* **2022**, *18*, 2983–2992.
- (73) Hoyer, C. E.; Hu, H.; Lu, L.; Knecht, S.; Li, X. Relativistic Kramers-Unrestricted Exact-Two-Component Density Matrix Renormalization Group. *J. Phys. Chem. A* **2022**, *126*, 5011–5020.
- (74) Boettger, J. C. Approximate Two-Electron Spin-Orbit Coupling Term for Density-Functional-Theory DFT Calculations Using the Douglas-Kroll-Hess Transformation. *Phys. Rev. B* **2000**, *62*, 7809–7815.
- (75) Ehrman, J.; Martinez-Baez, E.; Jenkins, A. J.; Li, X. Improving One-Electron Exact-Two-Component Relativistic Methods with the Dirac-Coulomb-Breit-Parameterized Effective Spin-Orbit Coupling. J. Chem. Theory Comput. 2023, 19, 5785–5790.
- (76) Liang, W.; Fischer, S. A.; Frisch, M. J.; Li, X. Energy-Specific Linear Response TDHF/TDDFT for Calculating High-Energy Excited States. *J. Chem. Theory Comput.* **2011**, *7*, 3540–3547.
- (77) Lestrange, P. J.; Nguyen, P. D.; Li, X. Calibration of Energy-Specific TDDFT for Modeling K-Edge XAS Spectra of Light Elements. *J. Chem. Theory Comput.* **2015**, *11*, 2994–2999.
- (78) Kasper, J. M.; Williams-Young, D. B.; Vecharynski, E.; Yang, C.; Li, X. A Well-Tempered Hybrid Method for Solving Challenging Time-Dependent Density Functional Theory (TDDFT) Systems. J. Chem. Theory Comput. 2018, 14, 2034–2041.
- (79) Jenkins, A. J.; Liu, H.; Kasper, J. M.; Frisch, M. J.; Li, X. Variational Relativistic Two-Component Complete-Active-Space Self-Consistent Field Method. *J. Chem. Theory Comput.* **2019**, *15*, 2974–2982.
- (80) Hu, H.; Jenkins, A. J.; Liu, H.; Kasper, J. M.; Frisch, M. J.; Li, X. Relativistic Two-Component Multireference Configuration Interaction Method with Tunable Correlation Space. *J. Chem. Theory Comput.* **2020**, *16*, 2975–2984.
- (81) Sauri, V.; Serrano-Andrés, L.; Shahi, A. R. M.; Gagliardi, L.; Vancoillie, S.; Pierloot, K. Multiconfigurational Second-Order Perturbation Theory Restricted Active Space (RASPT2) Method for Electronic Excited States: A Benchmark Study. *J. Chem. Theory Comput.* 2011, 7, 153–168.